Journal of Computational Physics **165,** 261–287 (2000)
doi:10.1006/jcph.2000.6615, available online at http://www.idealibrary.com on IDEAL®

Application of Double Fourier Series to the Shallow-Water Equations on a Sphere

Hyeong-Bin Cheong

Department of Environmental Atmospheric Sciences, Pukyong National University, 599-1 Daeyeon-3-dong Nam-gu, Pusan, 608-737, Korea

Received January 4, 2000; revised August 23, 2000; published online November 3, 2000

The spectral transform method using a double Fourier series as orthogonal basis functions as in Cheong (2000, *J. Comput. Phys.* **157**, 327) is extended to the solution of the shallow-water equations on a sphere. A spectral filter which mimics the implicit diffusion process with the third-order Laplacian operator is applied to the spectral components of predicted variables to prevent the aliasing error or nonlinear instability. For a predicted variable the spectral filter needs only about $76N^2$ operations with N being the zonal and meridional wavenumber truncation. The use of the filter even at every time step does not deteriorate the computational efficiency of the double-Fourier-series model, which comes from the availability of FFTs. The filter requires an additional memory for only $6N^2$ elements, so the total memory space of $O(N^2)$ is sufficient in the present model. Along with the incorporation of the polar filter, the semi-implicit time-stepping procedure contributes to a significant increase in the time-step size.

A standard test set proposed by Williamson *et al.* (1992, *J. Comput. Phys.* **102**, 211) is used to evaluate the errors associated with the new method for various resolutions. It is shown that as a whole the accuracy of the method is comparable to that of spherical harmonics model (SHM) though the present method provides more accurate time integration for some cases but does not for other cases. A long time-integration far beyond the period specified in the standard test set also illustrates almost the same accuracy as that given by the SHM. The relative efficiency of the method to the SHM appears from the resolution of 256×128 transform grids, and it becomes significant for resolutions higher than 512×256. The computational efficiency is expected to increase further with an improved FFT algorithm. The test results suggest that the new method could be extended to three-dimensional numerical models used for weather prediction.

Key Words: double Fourier series; shallow-water equations; spectral method; spectral filter; weather prediction.

0021-9991/00 $35.00

1. INTRODUCTION

Cheong [3] showed that the spectral transform method using a double Fourier series (half-ranged sine or cosine series in the meridional direction) as orthogonal basis functions can be successfully applied to the time integration of the vorticity and advection equations on a spherical domain with accuracy and efficiency. The double-Fourier-series model (DFM) has several advantages over the spherical harmonics model (SHM), which is the most commonly accepted atmospheric general circulation model [7], including computational efficiency, a uniform grid interval, and a memory requirement of only $O(N^2)$ elements. The operation count for the method is in general $O(N^2 \log N)$ while it is $O(N^3)$ for the SHM. The basis functions defined on transform grids, consisting of $O(N^3)$ elements, are no longer necessary in the method. In addition, both the orthogonality and orthonormality among the basis functions are better than those for the spherical harmonic functions. As in the spherical harmonics model [9], computational time can be saved to a large extent through the reduction of zonal transform grids in polar regions. One of the most important features of the DFM in Cheong [3], which does not exist in other double-Fourier-series models (e.g., [1, 20]), is the invertibility of the elliptic equation with $O(N^2)$ operations.

The double-Fourier-series model used in Cheong [3] has a minor point as well that the spherical harmonics filter (SHF) should be employed to eliminate nonlinear instability. The operation count for the filter is just N^3. Therefore the use of it at every time step deteriorates the efficiency of the DFM. Moreover, the eigensolutions of the Laplacian operator must be calculated for each zonal wavenumber and stored to be used as a spectral filter (the storage for N^3 elements is necessary). Of course, different sets of eigensolutions are needed when the resolution of the numerical model is altered. Although in the test calculations using the advection and vorticity equations Cheong [3] showed that the intermittent use of a SHF is sufficient for the prevention of nonlinear instability, whether it also works for more general cases is not made clear. Even though such a method works for these cases, it will be desirable to construct a simpler spectral filter that can provide the needed accuracy and stability of the model.

A double Fourier-series expansion over the sphere can also be found in the works of Boer and Steinberg [1] and Spotz *et al.* [20], where the meridional Fourier expansion is carried out along the great circle passing over the poles in order to keep the 2π-periodicity. For the method of Boer and Steinberg [1] a constraint on the spectral coefficients is necessary so as to satisfy the pole condition that the amplitude of the zonal wave component must vanish at the poles. A long time integration of nonlinear equations with this method cannot be accomplished because the spectral coefficients do not satisfy trivially the necessary condition. However, the pseudospectral method of Spotz *et al.* [20] does not need any constraint like this because the Fourier transform on meridians is taken only when the differentiation on grid points is carried out. Nevertheless, the nonlinear instability is unavoidable in this method without using a well-designed filter. Spotz *et al.* demonstrated that a spherical harmonics projection operator (SHPO; also commonly referred to as "a spherical harmonics filter" [23]) can be a cure for such a numerical instability. An efficient SHPO which interpolates the grids onto the Gaussian latitudes was introduced by [11]. A flexible SHPO with a reduced $O(N^3)$ operation applicable to an arbitrary distribution of latitudinal points has been recently developed [23]. In principle, time savings through the reduction of zonal transform grids in polar regions cannot be achieved in the pseudospectral method, in contrast to the method of Cheong [3].

In an attempt to overcome the severe degradation of performance at high resolutions for SHM, recently several new methods [19, 21, 24] which employ coordinate systems other than longitude–latitude have also been developed. The coordinate systems used there are capable of providing a uniform grid resolution over the sphere. They were found to produce an accurate and stable time integration for time-dependent nonlinear differential equations with substantial time savings for high resolutions. One of the most notable features of these new methods is the feasibility of local mesh refinement, although the assessment of accuracy and performance in such a case has not been reported yet. For these methods, the inversion of elliptic equations is not possible or needs a rather complicated numerical procedure such as an iteration method.

In this study, we extend the method of Cheong [3] to the shallow-water equations with the standard test suite proposed by Williamson *et al.* [26], which were used by various authors [10, 19, 20, 24] to assess the accuracy or stability of numerical methods. Computational efficiency is of great concern for DFM along with accuracy and simplicity. With this in mind, we introduce a spectral filter consisting of high-order diffusion operators rather than use the SHF of Cheong [3], because we want to implement a filter that needs only $O(N^2)$ operations and storage of the same order. While the SHF in [3] provides a sharp cutoff of the spherical harmonics whose total wavenumber is higher than the prescribed wavenumber, the diffusion-operator filter (hereafter called simply the "spectral filter") produces a smooth response with the horizontal scale, as the term diffusion would indicate.

The remainder of the paper consists of four sections: Section 2 describes the procedure to get the spectral forms of the shallow-water equations on a sphere written in a vorticity–divergence scheme. Section 3 is devoted to the design of a spectral filter for the prevention of nonlinear instability. Test results of the method based on the standard test suite are presented in Section 4. The results of the extended time integration are also shown for a particular test case at the end of Section 4. A discussion and conclusions are given in Section 5.

2. SHALLOW-WATER EQUATIONS AND SPECTRAL REPRESENTATION

2.1. *Shallow-Water Equations*

The shallow-water equations using a vorticity–divergence scheme in flux form [22, 26] scaled by the radius a and inverse rotation rate Ω^{-1} of the earth are written as

$$\frac{\partial \zeta}{\partial t} = \frac{-1}{\sin^2\phi}\left[\frac{\partial}{\partial \lambda}U(\zeta + f) + \sin\phi\frac{\partial}{\partial \phi}V(\zeta + f)\right], \tag{2.1a}$$

$$\frac{\partial \delta}{\partial t} = \frac{+1}{\sin^2\phi}\left[\frac{\partial}{\partial \lambda}V(\zeta + f) - \sin\phi\frac{\partial}{\partial \phi}U(\zeta + f)\right] - \nabla^2\left[\Phi' + \Phi_s + \frac{U^2 + V^2}{2\sin^2\phi}\right], \tag{2.1b}$$

$$\frac{\partial \Phi'}{\partial t} = \frac{-1}{\sin^2\phi}\left[\frac{\partial}{\partial \lambda}U\Phi' + \sin\phi\frac{\partial}{\partial \phi}V\Phi'\right] - \bar{\Phi}\delta, \tag{2.1c}$$

where λ is longitude and $\phi = \text{latitude} + \pi/2$, $U \equiv u\sin\phi$ and $V \equiv v\sin\phi$ with u and v being the longitudinal and latitudinal component of the velocities, respectively, and

$f(\equiv -2\cos\phi)$ is the Coriolis parameter; Φ_s is the surface geopotential ($=gh_s$; g and h_s are the gravitational acceleration and topography, respectively); Φ' is defined as gh' with h' being the deviation of the fluid depth (h^*) from the time-invariant global-mean height ($\bar{h}$): $\Phi' = gh^* - \bar{\Phi}$ with $\bar{\Phi} = g\bar{h}$. The vorticity ζ and divergence δ are defined in terms of velocity components as

$$\zeta = \frac{1}{\sin^2\phi}\left\{\frac{\partial V}{\partial\lambda} - \sin\phi\frac{\partial U}{\partial\phi}\right\}, \tag{2.2a}$$

$$\delta = \frac{1}{\sin^2\phi}\left\{\frac{\partial U}{\partial\lambda} + \sin\phi\frac{\partial V}{\partial\phi}\right\}. \tag{2.2b}$$

Dividing the velocity into rotational and divergent components such that

$$U = -\sin\phi\frac{\partial\psi}{\partial\phi} + \frac{\partial\chi}{\partial\lambda}, \tag{2.3a}$$

$$V = +\sin\phi\frac{\partial\chi}{\partial\phi} + \frac{\partial\psi}{\partial\lambda}, \tag{2.3b}$$

we can express the vorticity and divergence in terms of the streamfunction and velocity potential:

$$\zeta = \nabla^2\psi, \tag{2.4a}$$

$$\delta = \nabla^2\chi, \tag{2.4b}$$

$$\nabla^2 \equiv \frac{1}{\sin^2\phi}\left\{\frac{\partial^2}{\partial\lambda^2} + \sin\phi\frac{\partial}{\partial\phi}\sin\phi\frac{\partial}{\partial\phi}\right\}. \tag{2.4c}$$

Shallow-water equations in flux forms are simpler and require less computations than those in advective forms. Although for a particular case such as the stationary Rossby–Haurwitz wave the flux forms provide a slightly decreased accuracy [3], we have found that the accuracy is rather insensitive to the detailed formulations of the governing equations for the standard test suite (see also [22]).

2.2. *Spectral Representation with a Double Fourier Series*

As in Cheong [3], a true scalar function is represented with the truncated double Fourier series. For example, the vorticity is expanded as

$$\zeta(\lambda,\phi,t) = \sum_{m=-M}^{M}\zeta_m(\phi,t)e^{im\lambda} \tag{2.5a}$$

$$\zeta_m(\phi,t) = \begin{cases} \sum_{n=0}^{N}\zeta_{n,m}(t)\cos n\phi & \text{for } m=0, \quad (2.5b)\\ \sum_{n=1}^{N}\zeta_{n,m}(t)\sin n\phi & \text{for odd } m, \quad (2.5c)\\ \sum_{n=1}^{N}\zeta_{n,m}(t)\sin\phi\sin n\phi & \text{for even } m(\neq 0), \quad (2.5d)\end{cases}$$

where $i=\sqrt{-1}$, $m(n)$ is the zonal (meridional) wavenumber, and $M(N)$ is the largest wavenumber for the zonal (meridional) direction. The spectral component $\zeta_{n,m}$ is obtained

by the half-ranged Fourier transform of either $\zeta_m(\phi, t)$ for $m = 0$ and odd m or $\zeta_m(\phi, t)/\sin\phi$ for even $m(\neq 0)$, for which only $O(N^2 \log N)$ operations are necessary.

The spectral coefficients for the streamfunction and velocity potential are obtained from those of the vorticity and divergence by solving Poisson's equation as illustrated in [3],

$$A\zeta = D\psi, \tag{2.6}$$

where A and D are tridiagonal matrices of $N/2 \times N/2$ or $(N/2+1) \times (N/2+1)$, and ζ and ψ are vectors of $N/2$ or $(N/2+1)$ elements consisting of the spectral components of the vorticity and streamfunction, respectively. If the vorticity (streamfunction) is given, the streamfunction (vorticity) is obtained by solving $\psi = D^{-1}A\zeta$ ($\zeta = A^{-1}D\psi$) with an efficient Gaussian elimination procedure which requires $O(NM)$ operations.

The spectral coefficients of the velocity components are calculated from the diagnostic relations in Eq. (2.3) with the meridional truncations one level above those of the streamfunction and velocity potential, respectively. The spectral form for even m $(\neq 0)$ differs from those for odd m and $m = 0$ because of the parity function attached to the sine series:

$$U_{n,m} = \begin{cases} im\chi_{n,m} + n\{\psi_{n+1,m} - \psi_{n-1,m}\}/2, & \text{even } m(\neq 0); \quad (2.7a) \\ im\chi_{n,m} + \{(n+1)\psi_{n+1,m} - (n-1)\psi_{n-1,m}\}/2, & \text{odd } m, m = 0; \quad (2.7b) \end{cases}$$

$$V_{n,m} = \begin{cases} im\psi_{n,m} + n\{\chi_{n-1,m} - \chi_{n+1,m}\}/2, & \text{even } m(\neq 0); \quad (2.7c) \\ im\psi_{n,m} + \{(n-1)\chi_{n-1,m} - (n+1)\chi_{n+1,m}\}/2, & \text{odd } m, m = 0. \quad (2.7d) \end{cases}$$

The nonlinear terms are evaluated by the transform method [16]. Detailed procedures for this including the location of transform grids can be found in [3]. The spectral forms of the vorticity and divergence equation are written as

$$\frac{d}{dt}\zeta_{n,m} = \begin{cases} -imX_{n,m} + \{(n-2)Y_{n+1,m} - (n+2)Y_{n-1,m}\}/2, & \text{even } m(\neq 0); \quad (2.8a) \\ -imX_{n,m} + \{(n-1)Y_{n+1,m} - (n+1)Y_{n-1,m}\}/2, & \text{odd } m, m = 0; \quad (2.8b) \end{cases}$$

$$\frac{d}{dt}\zeta_{1,0} = -2Y_{0,0}; \tag{2.8c}$$

$$\frac{d}{dt}\delta_{n,m} = \begin{cases} imY_{n,m} - [\nabla^2\Phi']_{n,m} - E_{n,m} + \{(n-2)X_{n+1,m} \\ \quad -(n+2)X_{n-1,m}\}/2, & \text{even } m(\neq 0); \quad (2.9a) \\ imY_{n,m} - [\nabla^2\Phi']_{n,m} - E_{n,m} + \{(n-1)X_{n+1,m} \\ \quad -(n+1)X_{n-1,m}\}/2, & \text{odd } m, m = 0; \quad (2.9b) \end{cases}$$

$$\frac{d}{dt}\delta_{1,0} = -[\nabla^2\Phi']_{1,0} - E_{1,0} - 2X_{0,0}; \tag{2.9c}$$

where $X_{n,m}$ and $Y_{n,m}$ are the spectral coefficients of the nonlinear terms $U(\zeta + f)/\sin^2\phi$ and $V(\zeta + f)/\sin^2\phi$, respectively, and $\delta_{n,m}$ and $E_{n,m}$ are those of the divergence and $\nabla^2\{\Phi_s + (U^2 + V^2)/2\sin^2\phi\}$. For the nonlinear terms, we have to get the velocities and the vorticity on the grid points by the inverse Fourier transform. The spectral form of the

TABLE I
The Resolution and Time-Step Size

Model	$N(=M)$	$K \times J$	Δt (s)
M20	20	64×32	1440
M42	42	128×64	720
M84	64	256×128	360

geopotential equation is given by

$$\frac{d}{dt}\Phi'_{n,m} = \begin{cases} -imA_{n,m} - \bar{\Phi}\delta_{n,m} + \{(n-2)B_{n+1,m} \\ \quad -(n+2)B_{n-1,m}\}/2, & \text{even } m(\neq 0); \quad (2.10a) \\ -imA_{n,m} - \bar{\Phi}\delta_{n,m} + \{(n-1)B_{n+1,m} \\ \quad -(n+1)B_{n-1,m}\}/2, & \text{odd } m,\ m = 0; \quad (2.10b) \end{cases}$$

$$\frac{d}{dt}\Phi'_{1,0} = -\bar{\Phi}\delta_{1,0} - 2B_{0,0}, \quad (2.10c)$$

where $\Phi'_{n,m}$ denotes the spectral transform of $\Phi'(\lambda, \phi)$ and $A_{n,m}$ and $B_{n,m}$ are the spectral coefficients of $U\Phi'/\sin^2\phi$ and $V\Phi'/\sin^2\phi$, respectively. The $(N+1, 0)$ component of the spectral coefficients corresponding to the meridional advection terms should be discarded [3].

The number of transform grids in longitude (K) and latitude (J) is set by $K \geq 3M+1$ and $J \geq (3N+1)/2$, respectively. These are appropriate conditions for the triangular truncation for spherical harmonics models. Table I presents the number of grids, the wave truncation, and the size of the time step used in this study. It should be emphasized that the aliasing error is inherent in the present model because the spectral expansion in Eq. (2.5) actually includes the wave components corresponding to the rhomboidal truncation. The numerical method to prevent the aliasing error or nonlinear instability will be presented in Section 3. As in previous studies [1, 3, 12, 20], the Fourier filter is used to filter out the higher zonal-wavenumber components from the Fourier transform of a field variable (e.g., $\zeta_m(\phi, t)$) in the vicinity of the poles. We adopt the type used by [3], in which the coefficients of the zonal Fourier transform such as $\zeta_m(\phi, t)$ are made zero provided that $m > (M-3)\sin\phi + 4$.

All the variables are set in double precision throughout the numerical experiments, for which floating points of 15 digits are available. To perform one time-step marching, 9 spectral transforms, either forward or inverse, are necessary. The spectral equations of (2.8)–(2.10) are time integrated with a leap frog scheme, using a constant time -increment Δt except for three initial time steps. To reduce the possibility of an initial shock, we begin with a forward scheme using a smaller time increment $\Delta t/4$, which is followed by two time steps of leap frog schemes with $\Delta t/4$ and $\Delta t/2$, respectively [14]. For some test cases we use a time filter [18] with a coefficient of 0.02 to suppress the computational mode.

2.3. *Semi-Implicit Time Integration and the Elliptic Equation*

To suppress the undesirable gravity oscillations and consequently to take a large time step, we introduce the semi-implicit method for time integration: The geopotential in the

divergence equation and the linear divergence term in the geopotential equation are dealt with implicity. The spectral representation for the semi-implicit method is illustrated with the formulas

$$\delta^{(p+1)} = \delta^{(p-1)} - 2\Delta t \nabla^2 \Phi'^{(p+1)} + G_\delta^{(p)}, \tag{2.11a}$$

$$\Phi'^{(p+1)} = \Phi'^{(p-1)} - 2\Delta t \bar{\Phi} \delta^{(p+1)} + G_\Phi^{(p)}, \tag{2.11b}$$

where the superscript (p) denotes the present time step while $(p-1)$ and $(p+1)$ denote the previous and the future one, respectively, and where $G_\delta^{(p)}$ and $G_\Phi^{(p)}$ are the remaining terms. These can be rearranged into a Helmholtz-type elliptic equation for the divergence, which is solved easily through the inversion of the tridiagonal matrix [3]

$$(1 - \varepsilon \nabla^2)\delta^{(p+1)} = H, \tag{2.12}$$

where $\varepsilon = \bar{\Phi}(2\Delta t)^2$ and H is the forcing function to be determined from Eqs. (2.11).

Since the divergence is expressed as a Laplacian of the velocity potential as in Eq. (2.4b), its global mean should vanish. Therefore the global mean of H should also vanish. In the course of the time-marching procedure, however, this cannot always be satisfied trivially, because of machine rounding errors. Therefore, we have to subtract the global mean from H (see Eq. (3.10) in [3] for the global averaging) prior to inversion of the elliptic equation. With this modified forcing function, $\delta_{0,0}^{(p+1)}$ may have an arbitrary value as a solution, but it should be changed to meet the condition that the global mean is zero, i.e.,

$$w = -\sum_{n=1}^{N/2} \left[\delta_{2n,0}^{(p+1)} / (1 - (2n)^2)\right], \quad w \to \delta_{0,0}^{(p+1)}.$$

For the same reason, the global mean of the vorticity must be eliminated from the predicted value.

If we are to invert a Helmholtz-type elliptic equation in which the forcing function does not necessarily vanish (this is the case of spectral filtering in Section 3), the above procedure to get a solution is subject to a minor change. We first remove the global average, say $\bar{H}$, from the forcing function prior to inversion. After inversion, the spectral components $(n, m) = (0, 0)$ of the inverted variable should be rearranged in such a way that its global mean becomes $\bar{H}$. The necessity of the manipulations with respect to the $(0, 0)$ component arises from the matrix structure that all the elements of the first column in D as in Eq. (2.6) vanish for even modes of $m = 0$. An alternative method for the inversion of this case can be found because the spectral components are represented exactly as the sum of Legendre polynomials for $m = 0$ (see also Section 3). The detailed procedure for the alternative method is shown in the Appendix. The increase in the computational burden due to this method is almost negligible. Both methods will give results similar to each other in principle. It has been found, however, that the method in the Appendix gives more accurate results than that stated above. So we adopt the method described in Appendix for the inversion of the even mode of $m = 0$.

3. SPECTRAL FILTERING

3.1. *Eigenvalues and Eigenvectors of the Laplacian Operator*

With the spectral representations in Section 2, the Laplacian operator can be written in a standard eigensystem (e.g., [3]). Similar eigensystems and their eigensolutions, discretized with double Fourier series which are different from those adopted in this study, are discussed in Orszag [17] and Boyd [2]. In principle, for fixed m ($\geq$3) there are $m-1$ eigenmodes for odd m and $m-2$ for even m from the last (i.e., smallest meridional scale) that are not identical to the (surface) spherical harmonics (i.e., exact eigensolutions of the Laplacian operator). This is easily understood if it is remembered that spherical harmonics may be represented as a cosine series with the m-th power of the sine of the colatitude [13]. All modes for m ($\leq$2) are identical to those of spherical harmonics. In other words, only spherical harmonics within the triangular truncation are calculated correctly with the double-Fourier-series expansion. In the sense that the structures of spherical harmonics correspond to those of the Rossby–Haurwitz waves, which are the normal modes of the linearized vorticity equation in a quiescent environment [8], the wrong eigensolutions in the double-Fourier-series expansion may be called unphysical modes [25].

To see the difference of the calculated eigenvalues (C_l) of the Laplacian operator from the theoretical one ($-l(l+1)$) in detail, the ratio R_l defined as $\log[-C_l/l(l+1)]$ is presented in Fig. 1 for $M=N=64$. Here l is the total wavenumber-like index of the spherical harmonic functions; i.e., l equals the zonal wavenumber *plus* the number of nodal point between poles. The wave components lying on the line parallel to the diagonal running from left-up to right-down have the same l. It is noteworthy that the number of incorrect eigensolutions are smaller than was expected above (see also [2]) for the zonal wavenumbers larger than m_e(=30 in this case), and the contours of R_l exhibit steplike variation. The reasons for these differences are not yet clear. For the incorrect eigensolutions, the deviation from the theoretical value becomes severe as the zonal wavenumber decreases for fixed l and increases with l for fixed m. As one could expect, the unphysical mode gives

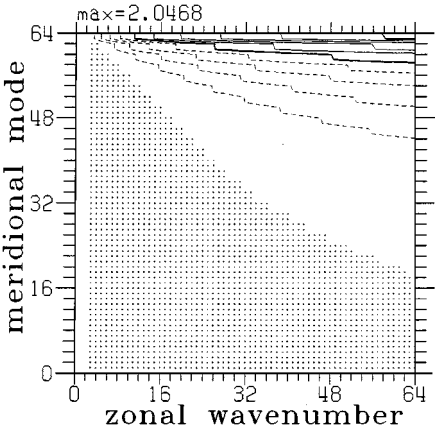

FIG. 1. Distribution of R_l defined as $\log[-C_l/l(l+1)]$, where C_l and $-l(l+1)$ are the calculated and theoretical eigenvalues of the spherical Laplacian operator for $M=N=64$, respectively. The definition of l is found in the text. Contour interval is 0.2 and the solid and dashed lines represent $R_l \geq 1.0$ and $R_l < 1.0$, respectively. The solid thick line is for $R_l = 1.0$ and the region marked with dots denotes $R_l = 0$. For the zonal wavenumber $m \leq 2$, $R_l = 0$ (not shown in this figure).

very poor orthogonality. (The orthogonality between two modes can be calculated with spectral coefficients following the formula for global integration of the quadratic term [3].)

The wrong eigensolutions will give rise to a numerical error when one evaluates the terms including the Laplacian operator or the nonlinear terms [3]. At the same time, it causes a severe restriction on the time-step size in the time-stepping procedure that includes the Laplacian operator [17]. The number of transform grids in this study was determined according to the 2/3 rule to prevent the aliasing error, which is an appropriate setting for the triangular truncation in a model of spherical harmonics base. Therefore the existence of the eigensolutions corresponding to wavenumbers beyond the triangular truncation may generate an aliasing error. For these reasons, it will be desirable to filter out the unphysical modes as well as the higher modes beyond the triangular truncation.

It is found that the SHF used in [3] should be applied at every time step to prevent the nonlinear instability for the shallow-water test cases proposed by [26]. This obviously deteriorates the efficiency of the DFM, in which the typical operation count is $O(N^2 \log N)$. This motivates us to find a more efficient filter than the SHF in [3].

3.2. *Spectral Filtering as a Diffusion Process*

In this study, we tried to design an efficient and simple spectral filter that is suitable not only for prevention of the nonlinear instability but also for accurate numerical integration. The simplest way to do this may be to consider a strongly scale-dependent diffusion process such that

$$\frac{\partial Q}{\partial t} = -c_1 \nabla^4 Q + c_2 \nabla^6 Q, \tag{3.1}$$

where Q is the variable to be filtered, c_1 and c_2 are positive constants, and all variables are nondimensional. To avoid severe restrictions on c_1 and c_2 (or the time-step size for this filtering process), the implicit time integration should be chosen. For the spherical harmonics model, implicit time integration with higher order Laplacian operators is trivial. However, it is not the case in this study. It must be accomplished by a successive inversion of Helmholtz equations. For convenience in the numerical procedure, we rewrite Eq. (3.1) with positive c_3 as

$$\frac{\partial Q}{\partial t} = -c_3 \nabla^2 Q + c_3 \nabla^2 Q - c_1 \nabla^4 Q + c_2 \nabla^6 Q. \tag{3.2}$$

This equation can be discretized in time with an implicit method except for one of the harmonic diffusion terms by assuming that one time step is Δt; this gives

$$Q^{(p+1)} = Q^{(p)} - c_3^* \nabla^2 Q^{(p)} + c_3^* \nabla^2 Q^{(p+1)} - c_1^* \nabla^4 Q^{(p+1)} + c_2^* \nabla^6 Q^{(p+1)}, \tag{3.3}$$

where $c_i^* = c_i \Delta t$ $(i = 1, 2, 3)$. Then $Q^{(p+1)}$ (hereafter denoted as Q^f), the filtered variable of $Q^{(p)} (\equiv Q)$, is obtained by solving successively the Helmholtz–type elliptic equations

$$(1 - c_4 \nabla^2)[(1 - c_5 \nabla^2)\{(1 - c_6 \nabla^2) Q^f\}] = (1 + c_3^* \nabla^2) Q, \tag{3.4}$$

where c_4, c_5, and c_6 are determined from c_1^*, c_2^*, and c_3^*. The numerical algorithm for the solution Q^f with spectral representation is shown in detail in [3]. To make Eq. (3.4) into a

simpler form, we first fix c_1^* and give $c_2^* = \gamma^3$ and $c_3^* = 3\gamma$ with $\gamma = \sqrt{c_1^*/3}$:

$$(1 - \gamma\nabla^2)^3 Q^f = (1 - 3\gamma\nabla^2) Q. \tag{3.5}$$

Now γ is the only parameter in this spectral filter and usually $\gamma \ll 1$. Thus the coefficient for the second term is much smaller than that for the first in Eq. (3.1). In other words, spectral filtering of this type is basically equivalent to using the biharmonic filter, but higher modes are more severely damped compared to the biharmonic filter. One can determine the filter viscosity based on physical reasoning, e.g., by specifying the damping rate of a certain mode, as is usually done in the SHM.

In Fig. 2 the amplitude ratio $R = (Q_{l^*}^m)^f / Q_{l^*}^m$ for various γ is presented, where m (=3, 4, . . . , 64) and l^* (=0, 1, 2, . . . , 64) are the zonal wavenumber and meridional mode number of the eigensolutions. The amplitude ratio must lie between 0 and unity. As is expected, the overall response increases (i.e., R becomes smaller) as γ increases, and it increases with both m and l^*. With $\gamma = (5 \cdot 2\pi)^{-1/3}/(64 \cdot 65)$ the strongest response for which the amplitude ratio of the filtered mode to the unfiltered is smallest reaches

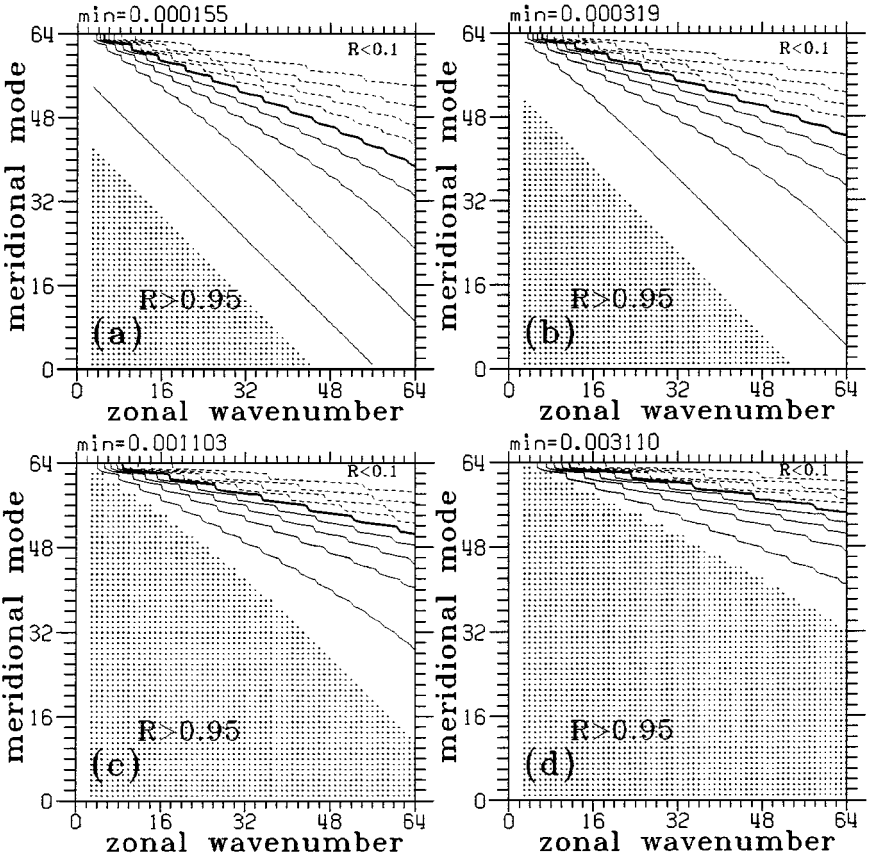

FIG. 2. Distribution of R defined as the ratio of the filtered to unfiltered eigensolutions of the Laplacian operator, for the zonal wavenumber $m \geq 3$. Contour interval is 0.1 and the solid and dashed lines represent $R \geq 0.5$ and $R < 0.5$, respectively. The solid thick line is for $R = 0.5$ and the region marked with dots denotes $R > 0.95$. The coefficients of the spectral filter γ for (a), (b), (c), and (d) are 7.62×10^{-5}, 5.28×10^{-5}, 2.81×10^{-5}, and 1.64×10^{-5}, respectively.

TABLE II
Coefficients of the Spectral Filter

	γ	
Model	Test cases 1, 5, and 6	Test case 7
M20	5.312×10^{-5}	10.624×10^{-5}
M42	2.112×10^{-5}	4.224×10^{-5}
M84	0.830×10^{-5}	0.166×10^{-4}

nearly 10^{-4}. When it is $\gamma = (500 \cdot 2\pi)^{-1/3}/(64 \cdot 65)$, the strong response is more or less concentrated at the larger m and l^*. One thing to be emphasized is that even though the total wavenumber is the same, the larger amplitude loss is observed for the smaller zonal wavenumber. This is the property of the spectral filter which is most different from those used in [3]. Although the steplike variation of the responses is also present in Fig. 2, it disappears for the modes within the triangular truncation even in the case that the filter viscosity γ is large (see Fig. 2a).

As will be seen later, if γ is chosen appropriately the nonlinear instability does not appear in a time-marching problem. Too large a value of γ will result in excessive damping of the low wavenumber while too small a γ may be not enough to prevent the nonlinear instability. In Table II, we present the coefficients of the spectral filter for various model resolutions, which are found to be appropriate in the test cases of the present study. Note that γ decreases with the resolution. In a qualitative sense the spectral filter resembles the implicit viscosity (or diffusivity), but they are different from each other particularly in the case where semi-implicit time stepping is incorporated.

Let us consider the computational efficiency of the filter. Application of the filter to the variable Q with spectral representation requires performing three inversions and a forward operation of the Laplacian operator. For the sake of the efficiency of the filter, prehandling of the matrices in Eq. (2.6) is necessary to prepare the modified matrices for each zonal wavenumber. The total memory space of $6N^2$ elements is sufficient for the modified matrices. Application of the filter to a field variable in the spectral space needs only the operation count of $(76N^2 + 36N)$. Before time marching of the prognostic variables, we apply the filter to the initial field. After the first time step, it is applied to the predicted variables at every time step, i.e., variables at time step $(p + 1)$.

4. TEST RESULTS

Williamson *et al*. [26] proposed a test suite for the numerical solutions of the shallow-water equations, consisting of seven cases: Four test cases have analytic solutions while the remaining three cases do not. Various error measures used to assess the accuracy of a new method are described in detail. For the cases which have no closed solutions, the errors should be measured as the differences of the solutions from those of high-resolution spherical harmonics models such as the NCAR T213. In this study, we produced the reference solutions from a T213 model which was independently coded by the author. Accuracy of the Legendre functions used in this code can be found in Cheong [3].

Detailed mathematical formulas for the standard test cases can be found in [26]. Here we describe the test cases as briefly as possible. For some test cases, the earth's rotation axis is

made to have an angle α from the coordinate axis to investigate the so-called pole problem which could be caused by using the spherical coordinate system. In addition to the standard test cases, an extra test result for test case 5 is presented in Section 4.3.

4.1. *Standard Test Cases 1–4*

Test case 1 is the advection of the cosine-bell height field with maximum value of 1000 m by the nondivergent super-rotation flow (the divergence field is made zero for this test case). The direction of the flow α is varied from 0 to $\pi/2$: The center of the cosine bell is advected along a great circle which makes an angle α with the equator. Some solutions using the double Fourier series are shown in [3] where a spherical harmonics filter was used. In this study, the results with the spectral filter described in Section 3 are presented. The advecting flow u_0 is given to be about 40 m/s which gives one evolution per 12 days. Figure 3a shows the error growths of $l_1(h)$ and $l_2(h)$ with time for $\alpha = \pi/2 - 0.05$ and M42. The signal of passing the north pole that was not present in the experiment with the SHF [3] is evident around day 3 for both $l_1(h)$ and $l_2(h)$, with a stronger signal for $l_1(h)$. $l_1(h)$ steadily increases before day 3 but after passing the north pole it does not vary significantly with time. The results for $\alpha = 0.05$ and $\pi/4$ exhibit an error level similar to that for $\alpha = \pi/2 - 0.05$, but the signal of passing the north pole disappears for $\alpha = 0.05$ and is weakened for $\alpha = \pi/4$. Figure 3b illustrates how the $l_2(h)$ error at day 12 varies with the model resolution. One can find a very good convergence rate of the solutions.

As in [3] where the SHF was used, the spatial structure of the calculated cosine bell is almost exactly overlapped with the theoretical cosine bell (not shown here). The spatial structure of the error field is also very similar to that in [3]. As in other numerical methods [10, 24], the most significant errors are found over the cosine bell and the spectral ringing is seen over the sphere. The conservation property of a numerical method is a very important factor. This is checked by taking the ratio $[h]_t/[h]_0$ where $[h]_t$ and $[h]_0$ are the global integral of height field at time t and initial condition, respectively. The ratio was found to remain on the order of 10^{-15} during one evolution for $\alpha = \pi/2 - 0.05$.

Test case 2 is the zonal geostrophic flow of super-rotation which is rotated poleward by an angle α. The geostrophic flow u_0 on the equator is about 40 m/s. The spectral filter is not

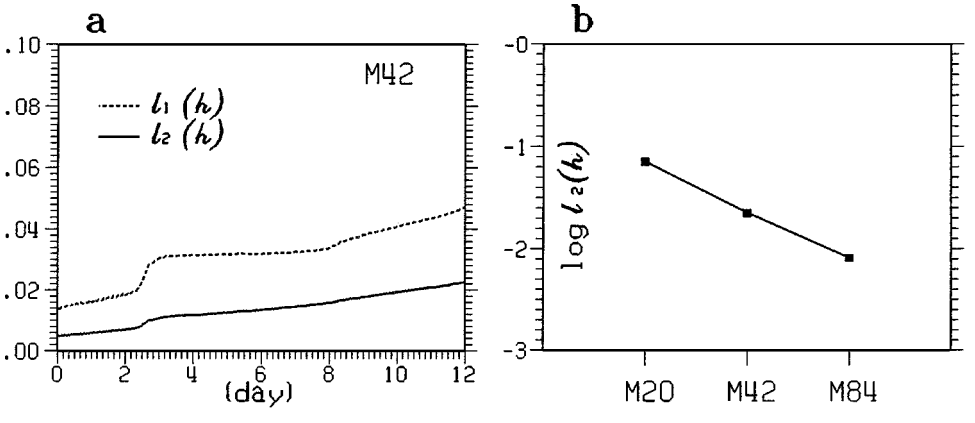

FIG. 3. (a) Time variation of $l_1(h)$ in dashed lines and $l_2(h)$ in solid lines for test case 1 with $\alpha = \pi/2 - 0.05$ and M42. (b) Sensitivity of $l_2(h)$ error at day 12 to the model resolution for $\alpha = \pi/2 - 0.05$.

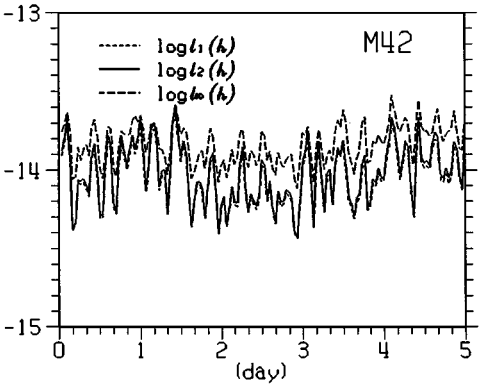

FIG. 4. Time variation of $l_1(h)$, $l_2(h)$, and $l_\infty(h)$ for test case 2 with $\alpha = \pi/2 - 0.05$ and M42.

used in this case. Figure 4 shows the time evolution of height errors $l_1(h)$, $l_2(h)$, and $l_\infty(h)$ for $\alpha = \pi/2 - 0.05$ and M42 on a logarithmic scale. Error levels remain on the order of 10^{-14} during the 5-day integration, exhibiting oscillation with time. Note that the lines for $l_1(h)$ and $l_2(h)$ almost perfectly overlap. The amplitude of oscillation reaches nearly one order for $l_1(h)$ and $l_2(h)$ while it remains in nearly half an order for $l_\infty(h)$. For $\alpha = 0.05$, however, the amplitude of oscillation is reduced to a significantly lower value as shown in Fig. 5a. These oscillations are due to sampling errors (see also [10, 24]). For $\alpha = 0.05$, $l_1(h)$ and $l_2(h)$ increase slowly with time, but $l_\infty(h)$ does remain almost at the same error level during the 5-day integration.

Figure 5b shows the time evolution of the $l_2(h)$ error for M20 and M84 with $\alpha = \pi/2 - 0.05$. It is interesting to note that the accuracy decreases with the resolution, which is also found in other methods (e.g., Spotz *et al.* [20]): For the experiment with M20 the error increases with time, but unlike M42 the amplitude of the oscillation is very small. For M84, the amplitude of oscillation is smaller than the M42 case, while the error is larger than that for M42 by nearly one order. The increase of errors with resolution is attributable to the fact that the flow field is so simple that it can be represented only with the first mode of the meridional basis functions, and the roundoff errors associated with the matrix inversion as in Eq. (2.6) increase with the matrix size.

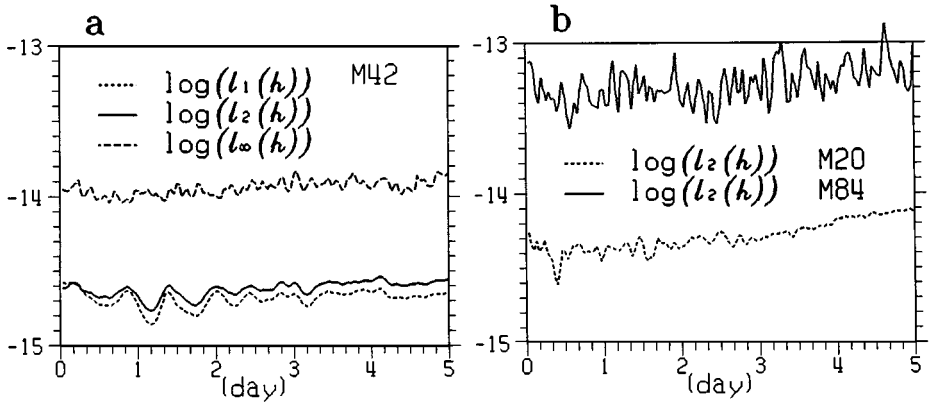

FIG. 5. (a) Time variation of $l_1(h)$, $l_2(h)$, and $l_\infty(h)$ for test case 2 with $\alpha = 0.05$ and M42. (b) Time variation of $l_2(h)$ for the model resolutions M20 (dashed line) and M84 (solid line) for the case $\alpha = \pi/2 - 0.05$.

Test case 3 is the zonal geostrophic flow with compact support. The initial flow and height field contain more meridional modes than the flow used in test case 2 because the meridional extent of the flow field is very narrow. So if the model resolution is low, the initial field cannot be expressed accurately. Spectral filtering was not done for this case. The initial height field should be obtained from the velocity field given. Unlike as in [26] where the height field is obtained by an integration, here it is calculated through matrix inversion, which is much simpler than the integration method. For brevity, we illustrate the procedure involved in the simple case where the rotation angle α is zero. The balance equation from which the height field is calculated is

$$u^2 \tan\theta + \frac{\partial \Phi'}{\partial \theta} + 2u = 0, \tag{4.1}$$

where θ is the latitude. With some manipulations, we can rewrite this equation as the second-order differential equation

$$\cos\theta \frac{\partial}{\partial \theta}\left[u^2 \sin\theta + \cos\theta \frac{\partial \Phi'}{\partial \theta} + 2u \cos\theta\right] = 0. \tag{4.2}$$

Then Φ' can be solved by a matrix inversion as described in [3], taking into consideration that the second term includes the Laplacian operator with zonal wavenumber of zero and the remaining terms constitute the forcing function in a Poisson's equation. In this procedure, the meridional truncation for $u^2 \sin\theta$ and $u \cos\theta$ must be $N + 1$, and Φ' has meridional modes up to $N + 2$. In a similar manner, the height field can be determined when the geostrophic flow is not parallel to the latitudinal circles, i.e., $\alpha \neq 0$.

Figure 6a shows the time evolution of height errors $l_1(h)$, $l_2(h)$, and $l_\infty(h)$ with $\alpha = \pi/3$ and M42. It can be seen that $l_\infty(h)$ is larger than both $l_1(h)$ and $l_2(h)$ by a factor of about one order. The errors increase sharply during the first eight hours, accompanied by a rather slow increase after that. Although $l_1(h)$ and $l_2(h)$ are oscillating with time, the amplitudes of oscillation decrease with time. The sensitivity of the error $l_2(h)$ to the model resolution is presented in Fig. 6b. Compared to the case of M42, the accuracy decreased by about four orders for M20 while it increased by about one and half order for M84.

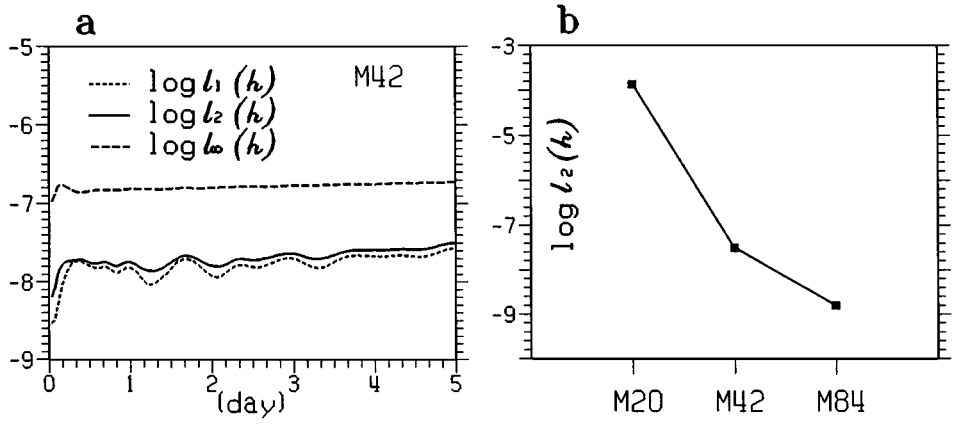

FIG. 6. (a) Time variation of $l_1(h)$, $l_2(h)$, and $l_\infty(h)$ for test case 3 with $\alpha = \pi/3$ and M42. (b) Variation of $l_2(h)$ with the model resolution at day 5 for $\alpha = \pi/3$.

Test case 4 is the forced nonlinear system with a translating low which is forced to advect zonally with either $u_0 = 20$ m/s or 40 m/s. In the standard test set [26], the forcing function is given with the velocity field, while the prediction variables used in this study are the vorticity and divergence. Since it is trivial to express the momentum forcing in terms of the vorticity and the divergence using the identities in Eqs. (2.2), the detailed procedure to get the forcing functions in the present scheme is not shown. When the forcing function is given in terms of the streamfunction (e.g., Eqs. 128 and 130 in [26]), the vorticity is obtained through a matrix inversion as in Eq. (2.6).

The forcing functions in this case are time dependent, and they also include the time derivatives. As stated in Section 2, the predicting scheme in this study is able to incorporate the semi-implicit method in the time-stepping procedure. The forcing terms are also treated semi-implicitly in order to keep the consistency in the numerical approach. For this purpose, the time derivatives in the forcing are incorporated in the model with a finite difference approximation rather than an analytic expression. A time filter is used in this test case, while the spectral filter was not introduced. The initial height field is not shown because it is indistinguishable from those in [10].

The height difference from the analytic solution for M42 at day 5 is illustrated in Fig. 7. Though the largest error is found over the translating low (the center of each figure), a fairly large error is also distributed to the north and east of it. It is also noted that the error field exhibits a wave-train-like structure for which the amplitude decreases with the distance from the center. The amplitude of the error in the $u_0 = 40$ m/s case is larger than that in the $u_0 = 20$ m/s case by a factor of about 5. Figure 8a presents the time evolution of the $l_2(h)$ error for $u_0 = 20$ m/s and 40 m/s respectively. It is noted that the lines do not have short time-scale fluctuations during the integration period [10, 24]. This might be attributable to the semi-implicit time-stepping procedure. Figure 8b illustrates the error convergence with the resolution. The error decreased by more than one order when the resolution increased from M20 to M42 while it decreased only by a factor of 2 when the resolution increased from M42 to M84.

It should be reported that the time filter affects the accuracy to a certain extent. For example, when the time filter is removed in this test case the error level is significantly lowered: With $u_0 = 40$ m/s, $l_2(h)$ errors at day 5 are 5.75×10^{-5}, 7.63×10^{-9}, and 2.01×10^{-12}

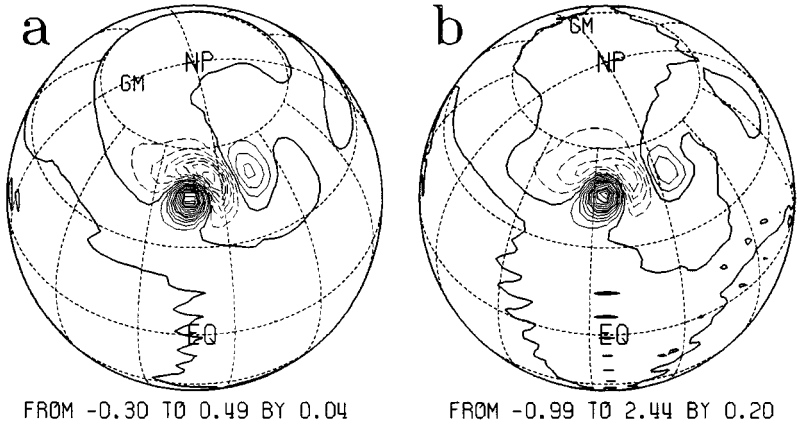

FIG. 7. Height error fields at day 5 for test case 4 with (a) $u_0 = 20$ m/s and (b) $u_0 = 40$ m/s for the M42 case. Positive (negative) values are in solid (dashed) lines.

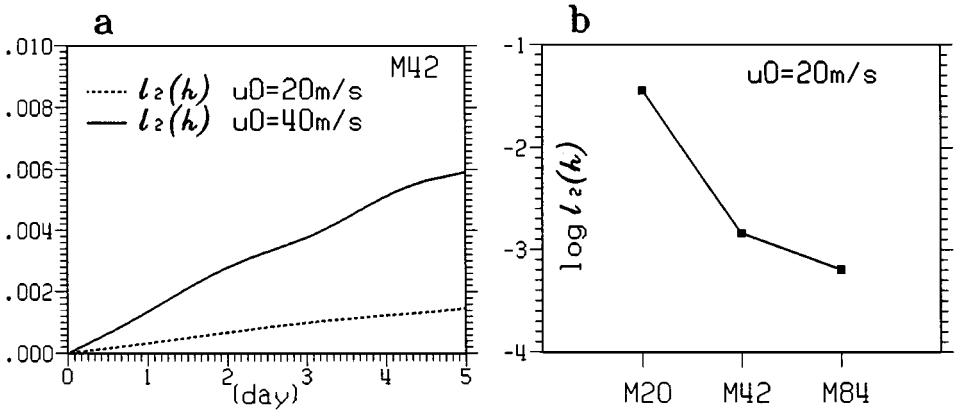

FIG. 8. (a) Time variation of $l_2(h)$ for test case 4 with M42. (b) Variation of $l_2(h)$ with the model resolution at day 5 for $u_0 = 20$ m/s.

for M20, M42, and M84, respectively. However, a long time integration without the time filter was found to be unstable.

4.2. *Standard Test Cases 5–7*

Test case 5 deals with the zonal flow over an isolated mountain 2000 m high, located at (90°W, 30°N), with $\alpha = 0$ and the equivalent depth $h_0 = 5960$ m. The initial zonal flow is of a super-rotation with the maximum wind speed being 20 m/s. Because the analytic solution is not available in this case, we have calculated the error as the difference from the solution provided by a high-resolution model, T213. A time filter is used for this and the remaining cases. Figure 9a shows the time variations of the globally averaged, normalized total-mass error $I(h)$ for M42 and M84. Note that the total mass increases with time for M84 while it decreases for M42. The accuracy for M84 increased by about half an order compared to M42. In Fig. 9b, the normalized total-energy error $I(TE)$, one of the second-order invariants without dissipation, is illustrated at the same resolutions as in Fig. 9a. The energy decreases monotonically with time and the energy-loss rate for M84 is about one-fifth of that for M42.

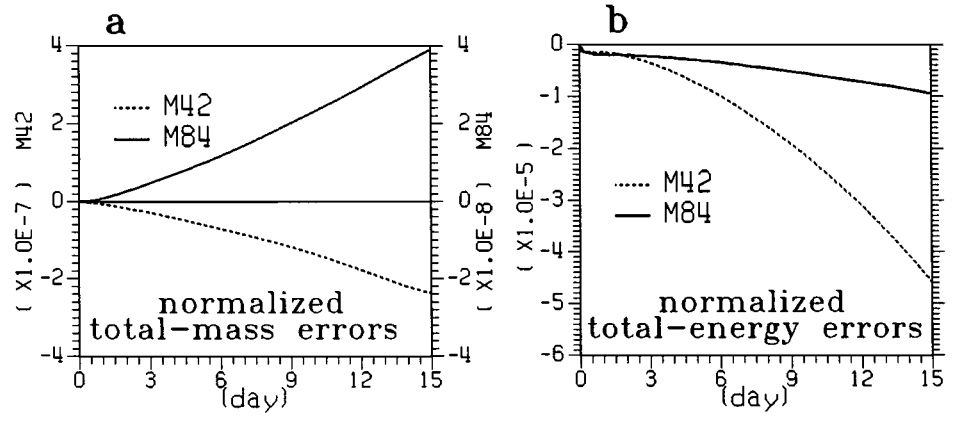

FIG. 9. (a) Time variation of the normalized total-mass error $I(h)$ for test case 5. Scale on the left (right) vertical axis is for M42 (M84). (b) Time variation of the normalized total-energy error.

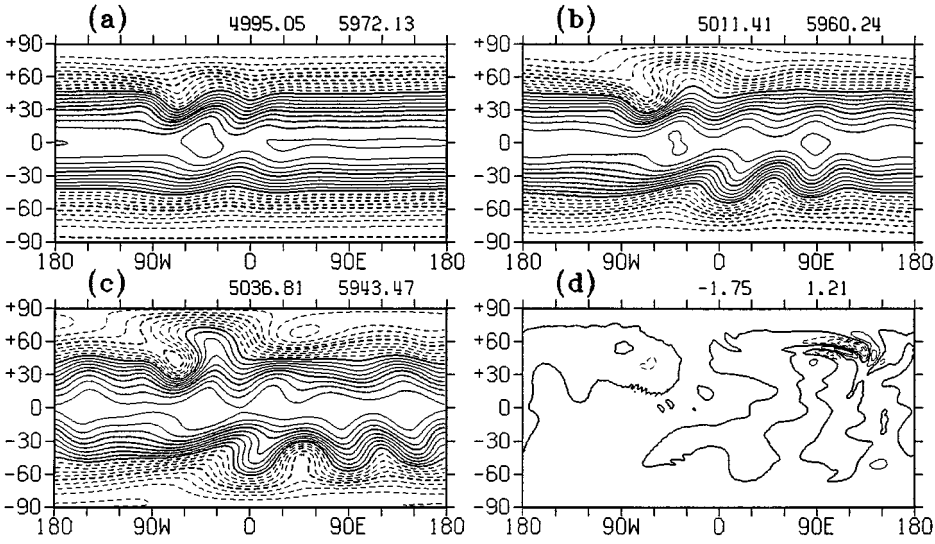

FIG. 10. Height field at (a) day 5, (b) day 10, and (c) day 15 for test case 5 with M84. (d) shows the height difference from T213 at day 15. Contour intervals for (a)–(c) are 50 m and solid (dashed) lines are for $h \geq 5500$ m ($h < 5500$ m). Contour interval for (d) is 0.4 m with positive (negative) values in solid (dashed) lines. Numerals over each map are the minimum and maximum values, respectively.

Figure 10 presents the spatial structure of the height field for M84 at 5, 10, and 15 days, along with the difference from the T213 model at day 15. A large difference is found in the remote area rather than over the topography, whose amplitude is less than 2 m. Though the height field also exhibits a quite large wave amplitude in the southern hemisphere, the error is fairly small there. One interesting feature in this figure is that the largest error exists in the region where the spatial variation of the height field is rather small. Just southward downstream of the topography, very small scale errors are distributed. We have found that they disappear with an enhanced spectral viscosity (not shown).

The normalized difference from the spherical harmonics model T213, $l_2(h)$, is given in Fig. 11. For M42 the error increases sharply in the first day, followed by a slow increase after that. The error for M84 steadily grows but is just 0.30×10^{-4} at day 15, which is

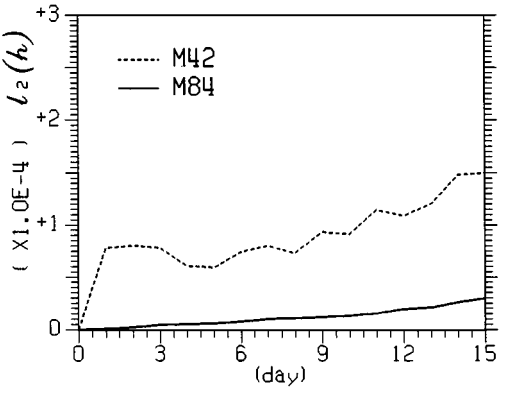

FIG. 11. Time variation of $l_2(h)$ for test case 5.

about one-fifth of that for M42. Not shown here is the normalized enstrophy error for M42, which shows a steady exponential decrease until day 12 except for the initial few days where it remains positive with a maximum value of 0.21×10^{-5}. After day 12 it shows a rather slow linear decrease. The normalized enstrophy errors at day 15 are 0.89×10^{-4} and 0.15×10^{-4} for M42 and M84, respectively.

Test case 6 is the stable Rossby–Haurwitz wave of the zonal wavenumber 4. In the absence of the divergence effect, it translates zonally, preserving the shape. The time variation of the normalized total-energy error $I(TE)$ during the first 14 days exhibits a nearly linear increase for both M42 and M84 (not shown), as was not observed in test cases 1–5. Such a behavior has also been reported in the numerical experiments using the spherical harmonics model (see Fig. 5–9b in [10]). Unlike as in [10], however, the short-scale fluctuation is nonexistent in the present model. As in most of the test cases shown above, the accuracy improves with the resolution of the model: $I(TE)$'s at day 14 are 3.37×10^{-4} and 1.82×10^{-4} for M42 and M84, respectively.

Figure 12 presents the spatial structure of the height field for M84 at days 0, 7, and 14, along with the difference from the spherical harmonics model T213. Large errors are distributed mainly in the middle and high latitudes. In general the negative anomalies have local peaks in the high latitudes while the positive anomalies show peaks around 30 degrees in both hemispheres. The time variation of $l_2(h)$, the normalized difference from the spherical harmonics model T213, is presented in Fig. 13. As a whole the error growth rate for M42 is larger than that for M84, particularly after day 11.

Test case 7 is the most realistic test where the observed flow fields at 500 hPa surface must be used as initial conditions. Any flow fields will be useful for this test provided that they are real observed data initialized by a proper method. Three cases are recommended to use by [26] for tests, 0000 GMT 21 December 1978, 0000 GMT 16 January 1979, and 0000 GMT 9 January 1979. These are characterized by either a strong flow over the

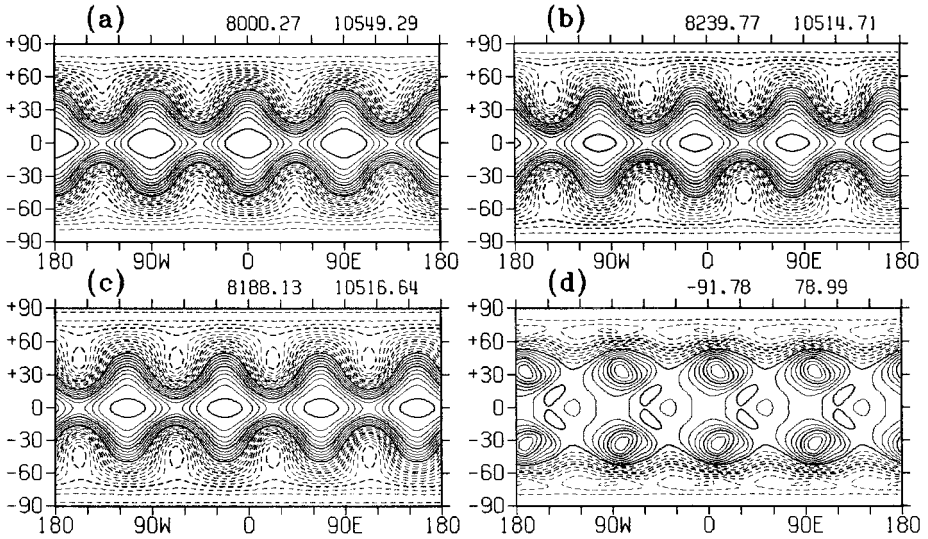

FIG. 12. Height field at (a) day 0, (b) day 7, and (c) day 14 for test case 6 with M84. (d) shows the height difference from T213 at day 14. Contour intervals for (a)–(c) are 100 m and solid (dashed) lines are for $h \geq 9500$ m ($h < 9500$ m). Contour interval for (d) is 10 m with positive (negative) values in solid (dashed) lines. Numerals over each map are the minimum and maximum values, respectively.

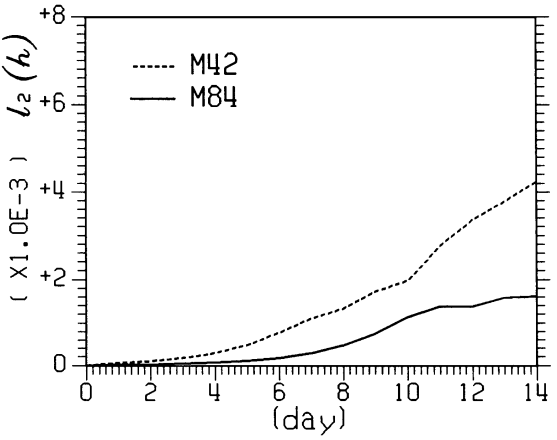

FIG. 13. Time variation of $l_2(h)$ for test case 6.

north pole or cutoff lows which develop into a typical blocking situation or a strong zonal flow.

In this study however, owing to the unavailability of the above data, we decided to use other recent data available from the Korean Meteorological Agency (KMA): Two cases of 1200 GMT 7 January 1999 and 1200 GMT 30 January 1999. One is characterized by a strong flow over the north pole which develops into a dipole structure over the eastern coast of the Eurasian continent, and the other is characterized by a large wave amplitude of zonal wavenumber 4 or 5. These are objectively analyzed data with a resolution of $1.875^\circ \times 1.875^\circ$. Since the initialization itself does not constitute the central issue of the test and needs additional work, the initialization process for the data is omitted. The initial height fields of the two cases are shown in Fig. 14 with a north polar stereographic projection.

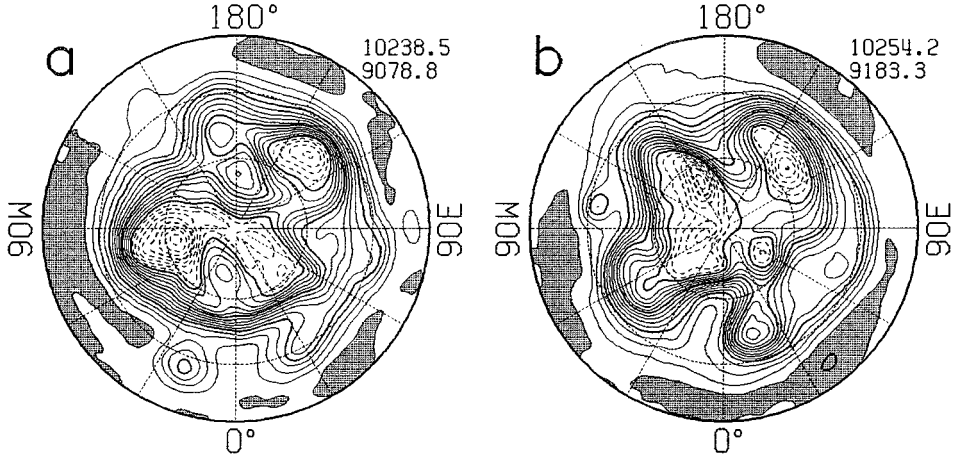

FIG. 14. Initial height fields of (a) 1200 GMT 7 January 1999 and (b) 1200 GMT 30 January 1999 used for test case 7. Contour intervals are 50 m and solid (dashed) lines are for $h \geq 9500$ m ($h < 9500$ m). Shaded region is for $h \geq 10{,}200$ m. Only the Northern Hemisphere is shown and the meridian and latitudinal circle are drawn every 30 degrees.

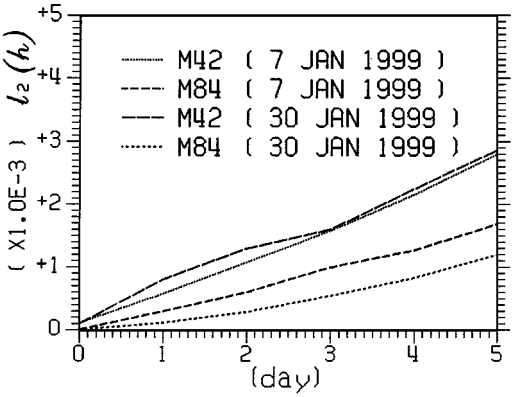

FIG. 15. Time variation of $l_2(h)$ for test case 7.

Figure 15 illustrates the time variation of $l_2(h)$ during the 5-day integration. The errors increase almost linearly with time for all cases. For two initial data the errors remain nearly in the same level and M84 gives better results than M42. Since for M42 the spatial resolution is lower than the given data and correspondingly the small-scale components of the observed data are removed from the initial condition, the error is as large as 1.0×10^{-4} even in the initial time. Figure 16 shows the height fields for different resolutions, along with the spatial distribution of height differences from the result with T213 at day 5 for the case of 7 January 1999. For both M42 and M84 the differences in high latitudes dominate over those in the low and middle latitudes. In particular, large-amplitude of errors are found over the polar region with M42.

In Fig. 17 we present a time series of height sampled hourly at selected grid points nearest to (31°N, 53°E) and (31°N, 90°E). Within the first day or so, one could observe short time-scale fluctuations with periods of about 6 hours and amplitudes of approximately 10–20 m. It is noteworthy that the amplitudes of them for M84 are larger than those for M42 and the fluctuations for both resolutions are almost in phase. In spite of the fact that the same initial data are used for M42 and M84, the selected height values are not identical to each other. This is because the sampling locations are different and the wave components retained in the models are not the same (see [26]).

4.3. *Test on the Long-Term Integration*

One important issue with regard to a numerical method is the feasibility of an accurate long-term integration without any numerical instability. The standard test suite consists of error estimates for rather short-term integrations. It will be also meaningful to show explicit evidence on the feasibility of a long-term integration far beyond the integration periods used in the standard test suite. We performed a 450-day integration for test case 5 with M42 and compared the result to the SHM of T42. In this case we take the time-step size $\Delta t = 1200$ s for both models. Figure 18 shows the time variation of the normalized total-energy errors. During the first month the error increases rather slowly. After this the error grows almost linearly with a large rate until about day 180, which is followed by a slower rate of increase. The errors for both models are comparable to each other although M42 gives a more accurate result than T42, as is expected from the result of the standard test.

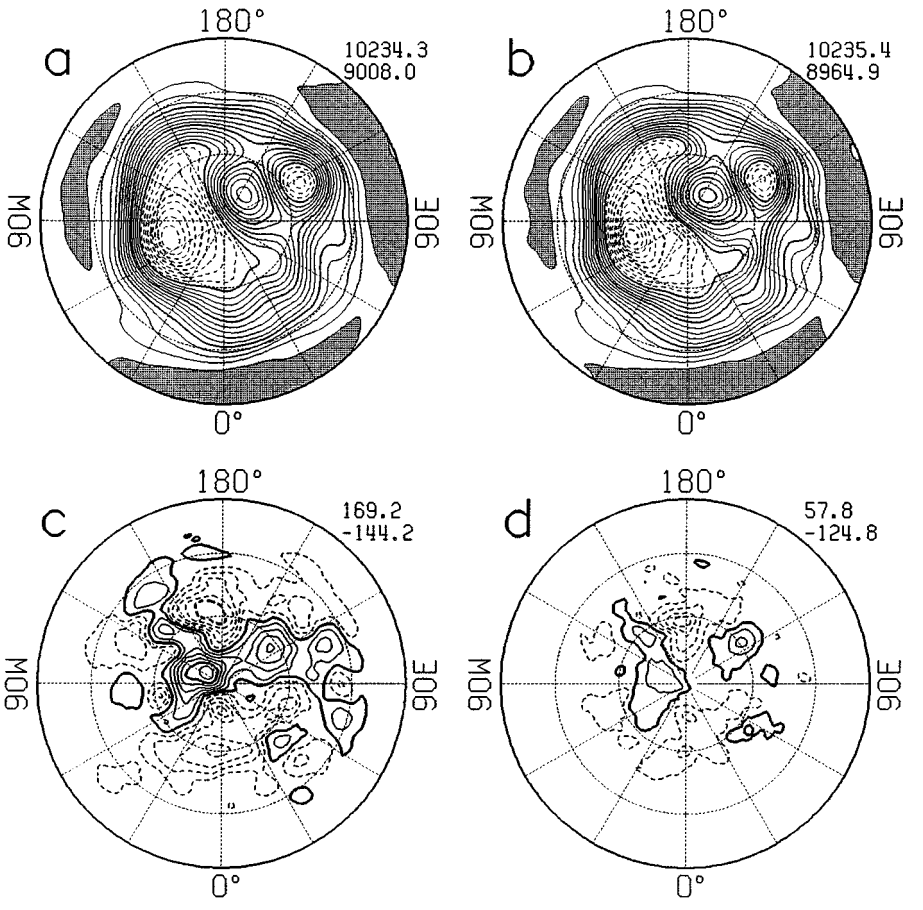

FIG. 16. Height fields at day 5 calculated by (a) M42 and (b) M84 with the initial field of 1200 GMT 7 January 1999 for test case 7. Height differences from T213 at day 5 are shown in (c) and (d) for M42 and M84, respectively. For (a) and (b) the contour intervals are 50 m and solid (dashed) lines are for $h \geq 9500$ m ($h < 9500$ m). Shaded region is for $h \geq 10{,}200$ m. Contour intervals for (c) and (d) are 25 m with positive (negative) values in solid (dashed) lines.

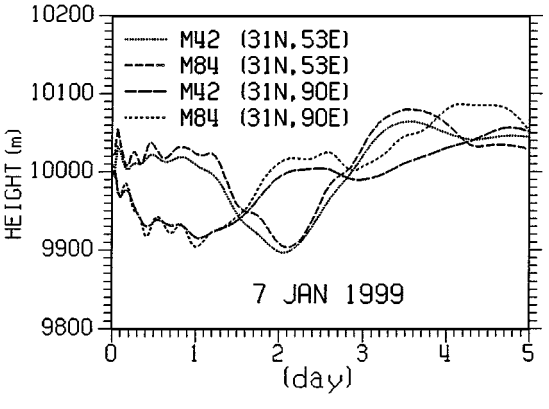

FIG. 17. Time series of height at selected grid points for test case 7.

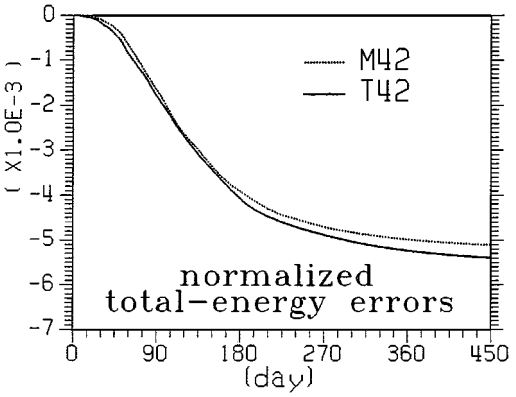

FIG. 18. Time variation of the normalized total-energy error for test case 5. Both results with M42 and T42 are compared for 450-day integrations.

In Fig. 19 the height fields are shown at selected days along with the topography. The height fields that are excited by the topographic forcing are well established with smooth variation over the sphere throughout the integration period. The time evolution of the height field suggests that the distinct three stages appearing in the error growth curve of Fig. 18

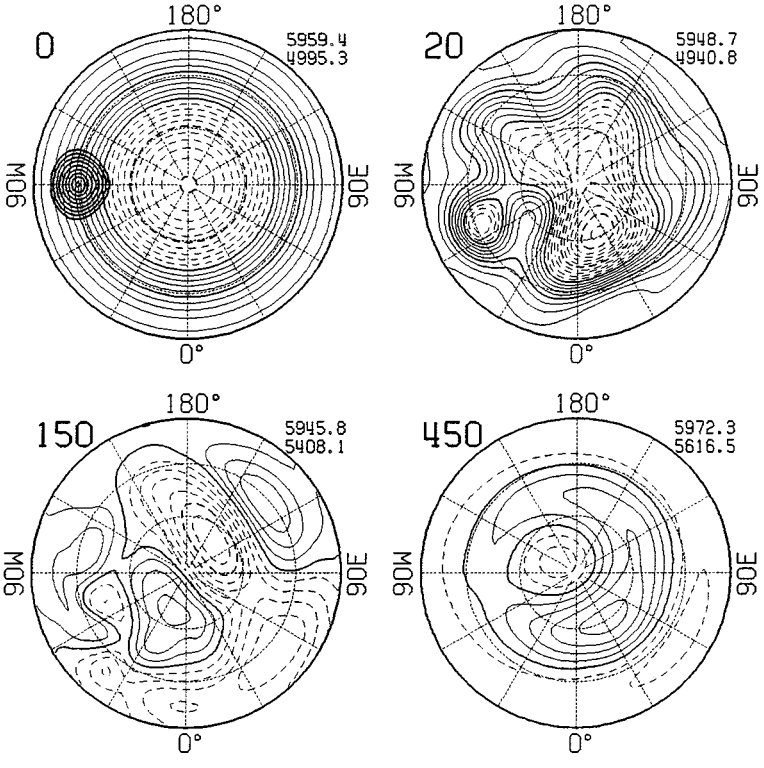

FIG. 19. Height fields at selected days (numerals on the top left) of long-term integration for test case 5. Topography is represented with thick solid lines with 200 m intervals in the first map. Contour intervals are 50 m and solid (dashed) lines are for $h \geq 5500$ m ($h < 5500$ m). Numerals over each map are the minimum and maximum values, respectively.

have direct relevance to the strength of the wave amplitude. For instance, when the height field (or flow field) is near the zonal state, the error growth rate remains small.

5. DISCUSSION AND CONCLUSIONS

In this study, the spectral transform method in [3] where the double Fourier series is adopted as basis functions was extended to the shallow-water model. The errors associated with the method are evaluated using the standard test suite proposed by [26]. We have found that as a whole the method gives comparable accuracy to the SHM for all cases considered [10, 24]. Test results are summarized in Table III along with the results of the SHM. For some cases the present method produces better results than the SHM (test cases 2, 5, 6 and 7) while it does not for other cases (test cases 1, 3, and 4). It is encouraging to note that the accuracy is improved by the present method for the test cases that have no analytical solutions (test cases 5–7). Among them the result of test case 7 is of particular importance because it consists of the observed flow.

A spectral filter consisting of high-order Laplacian operators (∇^4 and ∇^6) was designed and successfully used to prevent nonlinear instability. The application of the filter to a field variable in the spectral space needs $(76N^2 + 36N)$ operations. The memory space for $6N^2$ elements should be prepared for this filter. Other low-order filters such as harmonic or biharmonic-type may be used, for which less operations are necessary than that employed in this study. It should be remembered, however, that low-order filters are less effective in filtering out high wavenumber components beyond the triangular truncation. It is recommended that low-order filters be used when rather a strong damping is necessary in the model.

The relative efficiency of the present method can be estimated by comparing the operation count required for one time step. With $2J \times J$ transform grids ($J = 2^r$, where r is a positive integer), the total operation count for the SHM with the flux form is [4, 24]

$$C_{\mathrm{SHM}} = 5.9J^3 + 46.8J^2 \log_2 J + 92.8J^2,$$

where we did not take into consideration some minor terms. The present method needs 9 spectral transforms and 17 inversions at each time step. The inversions include spectral filtering for three predicted variables, semi-implicit time stepping, and procedures to get the streamfunction and velocity potential. The operation counts for the three major parts

TABLE III
Normalized L^2 Error for the Standard Test Cases with Comparison to Spherical Harmonics Models of T42 and T84

Model	Case 1	Case 2	Case 3	Case 4	Case 5	Case 6	Case 7
M42	.0220	1.1E-14	3.2E-08	.00146	1.5E-4	.0042	.0028
M84	.0082	6.2E-14	1.5E-09	.00064	3.0E-5	.0016	.0017
T42	.0110	2.0E-13	4.0E-10	.00082	9.6E-4	.0044	.0035
T85	.0050	3.0E-13	2.0E-13	.00040	7.7E-4	.0011	.0019

TABLE IV
The Ratio of the Operation Counts

J	$C_{\mathrm{SHM}}/C_{\mathrm{DFM}}$
32	0.68
64	0.90
128	1.28
256	1.99
512	3.29
1024	5.73
2048	10.32

can be written as follows:

$$\begin{aligned} \lambda\text{-FFT:} &\quad 46.8J^2 \log_2 J + 92.8J^2, \\ \phi\text{-FFT:} &\quad 31.5J^2 \log_2 J + 144J^2, \\ \text{Inversion:} &\quad 132J^2 + 102J. \end{aligned}$$

Then, the total operation count for the present method is

$$C_{\mathrm{DFM}} = 78.3J^2 \log_2 J + 368.8J^2,$$

where we again omitted the minor terms. The computational efficiency as measured by the ratio of operation counts $C_{\mathrm{SHM}}/C_{\mathrm{DFM}}$ is presented in Table IV. One finds that the advantage in computational efficiency appears from $J = 128$ and increases with the resolution of the model. Although the speedup of the efficiency is rather slow until $J = 256$, the relative efficiency is of significant level for the higher resolutions than this. It is certain that the advantage of the DFM will increase if we introduce a more efficient FFT algorithm than is currently used. Recently such a FFT algorithm, the so-called FFTW, can be found in Frigo and Johnson [5] and Frigo [6]. This algorithm is typically faster than all other publicly available FFT algorithms. Therefore, the method using double Fourier series could contribute to the enhancement of computational efficiency, particularly for high-resolution models. In addition to the computational efficiency, the present method requires a small storage of $O(N^2)$ elements, instead of $O(N^3)$ memory space as for the SHM.

In the present method the global mean is expressed as a sum of all spectral components with $m = 0$ while it is represented by only one spectral component for the SHM. For this reason, the global mean of a field variable, e.g., the vorticity or the divergence, does not necessarily vanish during the time integration in the present method, even though it should. Therefore we must change the value of the spectral component $(n, m) = (0, 0)$ to satisfy the condition of vanishing global mean. The modification of the $(0, 0)$ component does not affect the meridional differentiation of that variable, so no serious problem occurs in the course of time marching. Though being much larger compared to the SHM, the error in the normalized global-mean mass typically remains on the order of 10^{-7}–10^{-8} even for the fully nonlinear test cases simulated with moderate resolutions.

Finally we address an additional advantageous feature of the DFM not found in the methods of [19, 21, 24] where the longitude–latitude coordinate system is not used. One often wants to perform a numerical experiment where the L-fold symmetry (or cyclic boundary

condition) in the zonal direction is exactly maintained with $L \geq 1$. This is accomplished with ease in the new method, just by replacing $e^{im\lambda}$ by $e^{iLm\lambda}$ in Eq. (2.5a). But only odd integers of L are needed to keep the basis functions adequate for the pole conditions. It will be desirable in this problem to take the number of meridional wave components as sufficient to satisfy $N \geq LM$, if we consider the characteristics of eigensolutions of Laplacian operator stated in Section 2.

The test results presented in this study suggest that the double Fourier-series method could be extended to three-dimensional numerical models used for weather prediction.

APPENDIX

Inversion of the Elliptic Equation with Legendre Polynomials

Consider the inversion of an elliptic equation such that

$$(1 - \varepsilon\nabla^2)\delta_s = H_s, \tag{A.1}$$

where the subscript s denotes the even mode (symmetric with respect to the equator) of the zonal wavenumber $m = 0$. For this purpose we prepare a upper-diagonal matrix C of $(N/2 + 1) \times (N/2 + 1)$ which satisfies

$$P_{2n}(\cos\theta') = \sum_{r=0}^{n} C_{rn} \cos 2r\theta', \quad n = 0, 1, \ldots, N/2, \tag{A.2}$$

using the formula of Legendre polynomials (e.g., p. 80 of Moriguchi *et al.* [15])

$$P_{2n}(\cos\theta') = 2\sum_{r=0}^{n-1} \frac{(2r-1)!!(4n-2r-1)!!}{(2r)!!(4n-2r)!!} \cos 2(n-r)\theta' + \left\{\frac{(2n-1)!!}{(2n)!!}\right\}^2, \tag{A.3}$$

where θ' ($\equiv \pi - \phi$) is the colatitude and

$$(2n)!! = 2n(2n-2)\cdots 4 \cdot 2 \tag{A.4a}$$

$$(2n-1)!! = (2n-1)(2n-3)\cdots 3 \cdot 1. \tag{A.4b}$$

The coefficients q_{2n}'s (the coefficients of the Legendre polynomial expansion for H_s) can be calculated from the $H_{2n,0}$'s by combining Eq. (A.2) with the linear algebraic equations:

$$H_s = \sum_{n=0}^{N/2} H_{2n,0} \cos 2n\phi = \sum_{n=0}^{N/2} q_{2n} P_{2n}(\cos\theta'). \tag{A.5}$$

If we let d_{2n} be the coefficients of the Legendre polynomial expansion for δ_s we get

$$d_{2n} = q_{2n}/\{1 + \varepsilon 2n(2n+1)\}. \tag{A.6}$$

Then, the $\delta_{2n,0}$'s are obtained from the relations in Eqs. (A.2) and (A.5). Note that when the global mean of H vanishes (i.e., $q_0 = 0$), we have $d_0 = 0$.

The operational count for this procedure is only $N^2/2$, which is about 5% of the whole process associated with the inversion of all zonal wavenumber components.

ACKNOWLEDGMENTS

This work was supported by the Korea Research Foundation Grant KRF-99-D00448. The author thanks Dr. W.-J. Lee, the director of the numerical weather prediction division, Korean Meteorological Agency (KMA), for providing him with the observed data for test case 7. Anonymous reviewers are acknowledged for their useful comments.

REFERENCES

1. G. J. Boer and L. Steinberg, Fourier series on spheres, *Atmosphere* **13**, 180 (1975).
2. J. P. Boyd, The choice of spectral functions on a sphere for boundary and eigenvalue problems: A comparison of Chebyshev, Fourier and associated Legendre expansions, *Mon. Weather Rev*. **106**, 1184 (1978).
3. H.-B. Cheong, Double Fourier series on a sphere: Applications to elliptic and vorticity equations, *J. Comput. Phys*. **157**, 327 (2000).
4. O. K. Ersoy, *Fourier-Related Transforms, Fast Algorithms and Applications* (Prentice-Hall, Englewood Cliffs, NJ, 1997).
5. M. Frigo and S. G. Johnson, *The Fastest Fourier Transform in the West*, Technical Report MIT-LCS-TR-728, MIT Lab of Computer Science, 1997.
6. M. Frigo, A fast Fourier transform compiler, in *Proceedings of the 1999 ACM SIGPLAN Conference on Programming Language Design and Implimentation (PLDI)*, Atlanta, Georgia, 1999.
7. W. L. Gates, The atmospheric model intercomparison project, *Bull. Am. Meteorol. Soc*. **73**, 1962 (1992).
8. B. Haurwitz, The motion of atmospheric disturbances on the spherical earth, *J. Mar. Res. III* **3**, 255 (1940).
9. M. Hortal and A. J. Simmons, Use of reduced Gaussian grids in spectral models, *Mon. Weather Rev*. **119**, 1057 (1991).
10. R. Jakob, J. Hack, and D. L. Williamson, Spectral transform solutions to the shallow water test set, *J. Comput. Phys*. **119**, 164 (1995).
11. R. Jakob and B. K. Alpert, A fast spherical filter with uniform resolution, *J. Comput. Phys*. **136**, 580 (1997).
12. P. E. Merilees, The pseudospectral approximation applied to the shallow water equations on a sphere, *Atmosphere* **11**, 13 (1973).
13. P. E. Merilees, An alternative scheme for the summation of a series of spherical harmonics, *J. Appl. Meteorol*. **12**, 224 (1973).
14. K. Miyakoda, The method of numerical time integration of one dimensional linear equations and their inherited errors, *J. Meteorol. Soc. Jpn*. **38**, 259 (1960).
15. S. Moriguchi, K. Udagawa, and S. Hitotsumats, *Formulas for Mathematical Functions*, 5th ed. (Iwanami Shoten, Tokyo, 1990). [In Japanese]
16. S. A. Orszag, Transform method for the calculation of vector-coupled sums: Application to the spectral form of the vorticity equation, *J. Atmos. Sci*. **27**, 890 (1970).
17. S. A. Orszag, Fourier series on spheres, *Mon. Weather Rev*. **102**, 56 (1974).
18. A. J. Robert, The integration of a low order spectral form of the primitive meteorological equations. *J. Meteorol. Soc. Jpn*. **44**, 237 (1966).
19. C. Ronchi, R. Iacono, and P. S. Paolucci, The "cubed sphere": A new method for the solution of partial differential equations in spherical geometry, *J. Comput. Phys*. **124**, 93 (1996).
20. W. F. Spotz, M. A. Taylor, and P. N. Swartztrauber, Fast shallow water equation solvers in latitude–longitude coordinates, *J. Comput. Phys*. **145**, 432 (1998).
21. G. R. Stuhne and W. R. Peltier, Vortex erosion and amalgamation in a new model of large scale flow on the sphere, *J. Comput. Phys*. **128**, 58 (1996).
22. P. N. Swarztrauber, Spectral transform methods for solving the shallow-water equations on the sphere, *Mon. Weather Rev*. **124**, 730 (1966).

23. P. N. Swarztrauber and W. F. Spotz, Generalized discrete spherical harmonic transforms, *J. Comput. Phys.* **159**, 213 (2000).
24. M. Taylor, J. Tribbia, and M. Iskandarani, The spectral element method for the shallow water equations on the sphere, *J. Comput. Phys.* **130**, 92 (1997).
25. C. Temperton, *Normal Modes of a Barotropic Version of the* ECMWF Gridpoint Model, ECMWF International Report, **12**, European Center for Medium Range Weather Forecast, Reading, England, 1977.
26. D. L. Williamson, J. B. Drake, J. J. Hack, R. Jakob, and P. N. Swarztrauber, A standard test set for numerical approximations to the shallow water equations in spherical geometry, *J. Comput. Phys.* **102**, 211 (1992).